

REPORT DOCUMENTATION PAGE

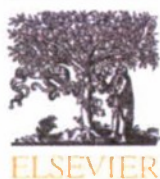
Form Approved
OMB No. 0704-0188

The public reporting burden for this collection of information is estimated to average 1 hour per response, including the time for reviewing instructions, searching existing data sources, gathering and maintaining the data needed, and completing and reviewing the collection of information. Send comments regarding this burden estimate or any other aspect of this collection of information, including suggestions for reducing the burden, to the Department of Defense, Executive Services and Communications Directorate (0704-0188). Respondents should be aware that notwithstanding any other provision of law, no person shall be subject to any penalty for failing to comply with a collection of information if it does not display a currently valid OMB control number.

PLEASE DO NOT RETURN YOUR FORM TO THE ABOVE ORGANIZATION.

1. REPORT DATE (DD-MM-YYYY) 02-06-2011		2. REPORT TYPE Journal Article		3. DATES COVERED (From - To)	
4. TITLE AND SUBTITLE Spatial Coherence Between Remotely-sensed Ocean Color Data & Vertical Distribution of Lidar Backscattering in Coastal Stratified Waters				5a. CONTRACT NUMBER	
				5b. GRANT NUMBER	
				5c. PROGRAM ELEMENT NUMBER 0601153N	
6. AUTHOR(S) M.A. Montes-Hugo, J. Churnside, Zhongping Lee, Richard W. Gould, Robert A. Arnone				5d. PROJECT NUMBER	
				5e. TASK NUMBER	
				5f. WORK UNIT NUMBER 73-9857-09-5	
7. PERFORMING ORGANIZATION NAME(S) AND ADDRESS(ES) Naval Research Laboratory Oceanography Division Stennis Space Center, MS 39529-5004				8. PERFORMING ORGANIZATION REPORT NUMBER NRL/JA/7330-09-0112	
9. SPONSORING/MONITORING AGENCY NAME(S) AND ADDRESS(ES) Office of Naval Research 800 N. Quincy St. Arlington, VA 22217-5660				10. SPONSOR/MONITOR'S ACRONYM(S) ONR	
				11. SPONSOR/MONITOR'S REPORT NUMBER(S)	
12. DISTRIBUTION/AVAILABILITY STATEMENT Approved for public release, distribution is unlimited.					
13. SUPPLEMENTARY NOTES					
14. ABSTRACT Detection of sub-surface optical layers in marine waters has important applications in fisheries management, climate modeling, and decision-based systems related to military operations. Concurrent changes in the magnitude and spatial variability of remote sensing reflectance (Rrs) ratios and submerged scattering layers were investigated in coastal waters of the northern Gulf of Alaska during summer of 2002 based on high resolution and simultaneous passive (MicroSAS) and active (Fish Lidar Oceanic Experimental, FLOE) optical measurements. Principal Component Analysis revealed that the spatial variability of total lidar backscattering signal (S) between 21 and 20 m depth was weakly associated with changes in the inherent optical properties (IOPs) of surface waters. Also based on a 250-m footprint, the vertical attenuation of S was inversely related to the IOPs (Spearman Rank Correlation up to -0.43). Low (arithmetic average and standard deviation) and high (skewness and kurtosis) moments of Rrs(443)/Rrs(490) and Rrs(508)/Rrs(555) ratios were correlated with vertical changes in total lidar backscattering signal (S) at different locations. This suggests the use of sub-pixel ocean color statistics to infer the spatial distribution of sub-surface scattering layers in coastal waters characterized by stratified conditions, well defined S layers (i.e., magnitude of S maximum comparable to near surface values), and relatively high vertically integrated phytoplankton pigments in the euphotic zone (chlorophyll a concentration N150 mg m ⁻²).					
15. SUBJECT TERMS vertical structure, inherent optical properties, statistical modes, ocean color, lidar					
16. SECURITY CLASSIFICATION OF:			17. LIMITATION OF ABSTRACT UL	18. NUMBER OF PAGES 10	19a. NAME OF RESPONSIBLE PERSON Richard W. Gould
a. REPORT Unclassified	b. ABSTRACT Unclassified	c. THIS PAGE Unclassified			19b. TELEPHONE NUMBER (include area code) 228-688-5587

20110804236



Spatial coherence between remotely sensed ocean color data and vertical distribution of lidar backscattering in coastal stratified waters

M.A. Montes-Hugo^{a,c,*}, J.H. Churnside^b, R.W. Gould^c, R.A. Arnone^c, R. Foy^d

^a Geosystems Research, Mississippi State University, MS 39529, USA

^b Earth System Research Laboratory, NOAA, Boulder, CO 80305 USA

^c Naval Research Laboratory, Code 7330, Stennis Space Center, NASA, MS 39529, USA

^d Shellfish Assessment, Alaska Fisheries Science Center, NOAA Fisheries, Kodiak, AK 99615, USA

ARTICLE INFO

Article history:

Received 17 December 2009

Received in revised form 24 April 2010

Accepted 28 May 2010

Keywords:

Vertical structure

Inherent optical properties

Statistical modes

Ocean color

Passive optical data

Backscattering

Lidar

Alaska

Coastal waters

ABSTRACT

Detection of sub-surface optical layers in marine waters has important applications in fisheries management, climate modeling, and decision-based systems related to military operations. Concurrent changes in the magnitude and spatial variability of remote sensing reflectance (R_{rs}) ratios and submerged scattering layers were investigated in coastal waters of the northern Gulf of Alaska during summer of 2002 based on high resolution and simultaneous passive (MicroSAS) and active (Fish Lidar Oceanic Experimental, FLOE) optical measurements. Principal Component Analysis revealed that the spatial variability of total lidar backscattering signal (S) between 2.1 and 20 m depth was weakly associated with changes in the inherent optical properties (IOPs) of surface waters. Also based on a 250-m footprint, the vertical attenuation of S was inversely related to the IOPs (Spearman Rank Correlation up to -0.43). Low (arithmetic average and standard deviation) and high (skewness and kurtosis) moments of $R_{rs}(443)/R_{rs}(490)$ and $R_{rs}(508)/R_{rs}(555)$ ratios were correlated with vertical changes in total lidar backscattering signal (S) at different locations. This suggests the use of sub-pixel ocean color statistics to infer the spatial distribution of sub-surface scattering layers in coastal waters characterized by stratified conditions, well defined S layers (i.e., magnitude of S maximum comparable to near surface values), and relatively high vertically integrated phytoplankton pigments in the euphotic zone (chlorophyll a concentration $>150 \text{ mg m}^{-2}$).

© 2010 Elsevier Inc. All rights reserved.

1. Introduction

Remote sensing reflectance above the sea surface ($R_{rs}(\lambda, 0+)$, where λ is the wavelength) and total lidar backscattering signal ($S(z)$) are theoretically connected in two ways. First, both depend on the volume backscatter function $\beta(\theta)$, where θ is the scattering angle. R_{rs} is directly proportional to backscattering coefficient ($b_b(\lambda)$), which is an inherent optical property (IOP) equal to the integral of β over all scattering angles greater than 0.5π . The amplitude ($A_{\beta}(z)$) of the total volume lidar backscattering is proportional to $\beta(\pi)$. The depth dependence of the lidar measurement is given by

$$S(z) = A_{\beta}(z)e^{(-2\alpha z)} \quad (1)$$

where $A_{\beta}(z)$ is the sum of the volume backscattering (β) contributions due to particulate (e.g., phytoplankton, zooplankton, fish) and dissolved (e.g., seawater) components, and α is the vertically attenuation

coefficient of lidar volume backscattering and independent of depth. Note that α is equal to the vertically diffuse attenuation of downward irradiance, K_d , if the lidar field of view is relatively wide (Gordon, 1982). The 17 mrad field of view of the lidar generally satisfied this condition (Churnside et al., 1998). Second, R_{rs} is inversely related to a , the total absorption coefficient (dissolved and particulate optical constituents), an IOP with major influence on K_d , and therefore responsible for lidar backscattering attenuation along the vertical component.

Current techniques to derive vertical shape of optical constituents based on R_{rs} have large uncertainties ($\sim 70\%$) or require prior knowledge of depth weighting functions (Piskozub et al., 2008; Zanaveld, 1982). As stated by Gordon and Brown (1975), the use of $R_{rs}(\lambda, 0+)$ spectra to infer vertical profiles of IOPs is impossible without *a priori* information. For example, even in the simple case of a single sub-surface peak of IOPs with a Gaussian profile, not all fitting parameters (i.e., amplitude, depth and width of peak) could be retrieved based solely on $R_{rs}(\lambda, 0+)$ measurements.

The use of Look-Up Tables (LUTs) of regionally and seasonally averaged IOPs (i.e., weighting averages), including dependence of depth, has been one approach to use surface observations of R_{rs} -derived chlorophyll a concentration (chl a) to obtain information

* Corresponding author. Geosystems Research, Mississippi State University, MS 39529, USA.

E-mail address: mmontes@ngi.msstate.edu (M.A. Montes-Hugo).

about the vertical structure of phytoplankton light absorption pigments in marine waters (Platt et al., 1988; Sathyendranath et al., 1995, hereafter SP method). In this case, different vertical profiles of IOPs are derived from ship-based chl *a* measurements by fitting to Gaussian curves. This technique has been a step forward to elucidate large-scale differences in the vertical structure of IOPs in case I waters (i.e., those where optical properties are defined by phytoplankton and covarying components). However, the SP method does not exploit other spatial statistical metrics (e.g., standard deviation, skewness, kurtosis) beyond the calculation of the arithmetic average of vertical distribution of IOPs and associated ocean color signatures derived from remote sensors.

The higher moments related to “peakedness” (kurtosis) and “symmetry” (skewness) of the probability distribution have been used in the ocean color community to characterize surface peaks of light-absorbing particulates (e.g., skewness and kurtosis are relatively high in *Trichodesmium* blooms) (Westberry & Siegel, 2006). Based on an analysis of the vertical microscale distributions of fluorescence, Mitchell et al. (2008) concluded that kurtosis and skewness of phytoplankton patch patterns were determined by multiple mechanisms (e.g., active migration of cells and formation of organic aggregates). Therefore, for a population of pixels, the statistical distribution of $R_{rs}(\lambda, 0+)$ ratios can potentially provide information about underwater perturbations of light fields.

In this study we performed aerial surveys using coincident passive and active optical measurements in coastal waters of the northern part of the Gulf of Alaska (NGOA) in order to answer the following scientific questions: How does the vertical structure of optical properties affect the spatial statistics of passive ocean color data measured above the ocean surface? Is a single lidar frequency sufficient to allow a ‘bridge’ with above-water radiance observations collected by multi-wavelength passive optical systems?

2. Methods

2.1. Study area

Eastern shelf waters of Afognak/Kodiak Islands (57.48°–58.04° N, 152.91°–151.67° W, Fig. 1) during late summer (August 17, 2002) are characterized by a well-developed pycnocline (median vertical density difference = 0.025 kg m^{-3} between 0 and 20 m in depth) (Appendix A,

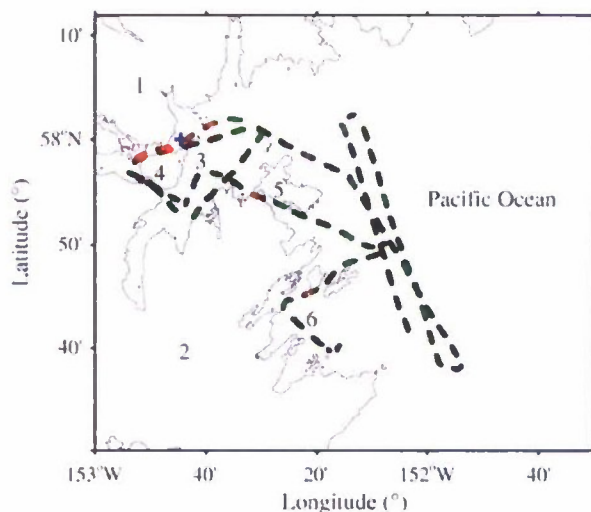


Fig. 1. Study area and aerial surveys. Concurrent FLOE and MicroSAS measurements (solid dots), case studies with HS (green dots) and IS (red dots) lidar waveforms (Table 3). Lidar data shown in Fig. 2 (blue cross). 1: Afognak Island, 2: Kodiak Island, 3: Marmot Bay, 4: Whale Island, 5: Spruce Island, 6: Chiniak Bay.

Fig. A1b) except in those areas influenced by local topographic upwelling (e.g., at the entrance of the Bays) or in particular regions previously vertically mixed by the passage of storms (Montes-Hugo et al., 2005). Likewise, greater phytoplankton concentrations as a function of depth were commonly observed just above the pycnocline depth as inferred from drastic vertical increase of CTD-derived chl *a* ($>2 \text{ mg m}^{-3}$) associated with major depth changes on seawater density ($>0.01 \text{ kg m}^{-3}$) (Appendix A, Fig. A1b). Therefore, these environments offer a mosaic of case studies characterized by waters with different vertical stratifications and consequently different vertical structures of optical properties and biogeochemical variables.

2.2. Aerial surveys and flight mission settings

Airborne $R_{rs}(\lambda, 0+)$ and $S(z)$ measurements were obtained between 12:54 and 14:30 pm local time and over waters deeper ($>50 \text{ m}$ depth) than penetration depth of the lidar system (Fig. 1). To avoid bottom-related reflectance and lidar backscattering contributions, only measurements over deep waters (i.e., $>50 \text{ m}$ bottom depth) were analyzed. Optimal flight weather conditions (i.e., cloud-free skies, wind speed $<4 \text{ m s}^{-1}$) were checked *a priori* based on local weather forecast (<http://www.wunderground.com/>) to maximize the number of comparisons between passive and active optical measurements. For the aerial survey, the altitude and speed were 300 m and 70 m s^{-1} , respectively. Based on these average flight characteristics, we collected a total of 3.0×10^4 passive radiometric measurements (upwelling and downwelling) and 1.66×10^5 lidar shots along a total distance of 332 km during 83 min . Airborne optical measurements were geo-located every 30 lidar shots (i.e., 1 s) during the full survey.

2.3. Optical determinations aboard the airplane

2.3.1. Passive measurements

Upwelling radiance ($L_u(\lambda)$) and downwelling irradiance ($E_d(\lambda)^{\text{plane}}$) were measured at 411, 443, 491, 509, 553, 665, and 780 nm to approximately match bands 1–7 of the spaceborne ocean color sensor SeaWiFS (Churnside & Wilson, 2008). The sensors (Micro Surface Acquisition System, MicroSAS, Satlantic) have bandwidths of 10 nm . The upwelling radiance sensor has a typical saturation radiance of $5 \mu\text{W cm}^{-2} \text{ nm}^{-1}$ and a field of view (FOV) of 3° (half angle) in air. Based on this FOV and a sampling rate of 6 observations per second, the pixel diameter of L_u MicroSAS measurements was 16 m (along-track) \times 200 m (across track). The MicroSAS irradiance sensor has a typical saturation irradiance of $300 \mu\text{W cm}^{-2} \text{ nm}^{-1}$ and a noise equivalent of $2.5 \times 10^{-3} \mu\text{W cm}^{-2} \text{ nm}^{-1}$. The orientation of the MicroSAS sensors were orthogonal to the sea surface plane (i.e., $L_u(\lambda)$ and $E_d(\lambda)^{\text{airplane}}$ were measured at 180° and 0° with respect to zenith).

2.3.2. Active measurements

Lidar backscattering measurements were obtained with a Fish Lidar Oceanic Experimental (FLOE) system (Churnside et al., 2001), looking down through a belly port of a twin-engine aircraft. FLOE detector was set up forward-looking and 15° off vertical to minimize specular reflections from the sea surface. In each lidar waveform, the sea surface was identified based on the large increase in signal when the pulse reached the surface. In this study, the lidar signature at the air-sea interface was clearly defined due to the absence of breaking-waves and fog. Hence, after eliminating the lidar propagation path in air (i.e., distance between airplane and sea surface), S can be computed for each lidar pulse from the vertical profiles of photocathode current by applying calibration factors related to optical system parameters (e.g., laser pulse energy, surface losses, receiver area, detector responsivity). The FLOE laser is linearly polarized and has beam divergence and receiver field of view of 17 mrad .

The receiver is polarized in the orthogonal plane and sampled at a rate of 10^9 samples per second. The dynamic range of the receiver is

sufficient to allow S measurements to a depth of nearly 100 m in the clearest ocean waters. In our coastal study area, the greater attenuation of laser energy reduced FLOE penetration depth to ~30 m on average. The green (532 nm) laser source was pulsed with an energy of 100 mJ, a pulse length of 15 ns, and a pulse repetition frequency of 30 Hz. This provides a pixel size of 5 m with an along-track spacing of about 2 m. The sampling vertical resolution into the water column was about 0.1 m.

2.4. Quality control of airborne optical determinations

In-situ airborne passive optical measurements were first screened to remove data affected by variable illumination caused by patchy cloud layers and by the presence of whitecaps. Additional filtering of optical data included the deletion of segments characterized by airplane turns (Fig. 1) and coinciding with drastic spatial changes on E_d and L_u magnitude due to changes on orientation of airborne sensors.

Pixels affected by clouds were screened and removed from further processing by comparing field $E_d(553)^{\text{airplane}}$ values against modeled $E_d(553)$ above the sea surface ($E_d(553)^{\text{model}}$). $E_d(553)^{\text{model}}$ estimates were computed based on a radiative transfer model (Hydrolight, Sequoia Scientific, Inc.) using local meteorological conditions reported by weather stations (visibility, sea level, atmospheric pressure, wind speed, relative humidity, Bob's P.C. Connection, Kodiak Island, Alaska, www.wunderground.com, precipitable water content, NOAA/GSD) or extracted from satellite imagery (e.g., total ozone from Total Ozone Mapping Spectrometer, TOMS) during the initial (21:54 GMT, August 17th) and final (23:30 GMT, August 17th) stage of the flight survey. Solar zenith angle was calculated using a solar position calculator and based on date and location (University of Oregon, Solar radiation monitoring laboratory). The airmass type criterion for choosing aerosol composition was based on wind direction data provided by Kodiak Island weather station. Aerosol thickness during this study was very small (<0.04) (SeaWiFS-derived 9 km resolution, wavelength = 865 nm) and is consistent with the lack of aerosol contributions due to volcanic plumes during this study (Alaska Volcano Observatory, http://puff.images.alaska.edu/puff_series_airroutes/Puff_20_years_1988_2008_series_conc.mpg).

Glint and foam contaminated pixels during airborne L_u measurements were screened based on Hydrolight simulations of L_u at 780 nm ($L_u(780)^{\text{model}}$) using the following settings: 1) atmospheric conditions similar to $E_d(553)^{\text{model}}$ runs but wind speed equal to zero (i.e., flat ocean), and 2) the range of in situ chl a values reported in this area (chl $a = 0.05$ to 10 mg m^{-3}). Magnitude of $L_u(780)$ measured outside the theoretical radiometric interval resulting from the above constraints was considered contaminated with glint or foam contributions and removed from further processing. Water scattering and absorption coefficients were derived from Smith and Baker (1981), and particulate scattering and absorption coefficients were computed from the Gordon and Morel empirical equations (Gordon & Morel, 1983; Morel, 1991), and interpolated phytoplankton specific absorption coefficients reported by Priour and Sathyendranath (1981). Only 11.8% of the original airborne data (i.e., 127 bins with 250-m resolution) corresponded to the ideal approximation 'clear skies and a glint-foam free ocean' based on modeled radiometric thresholds for $E_d(553)$ (range = 106.9 to $109.5 \text{ } \mu\text{W cm}^{-2} \text{ nm}^{-1}$) and $L_u(780)$ (range = $4.87 \cdot 10^{-2}$ to $8.86 \cdot 10^{-2} \text{ } \mu\text{W cm}^{-2} \text{ nm}^{-1} \text{ sr}^{-1}$).

2.5. Atmospheric correction

A quasi-single-scattering approximation (Rayleigh-aerosol multiple scattering ignored) was used to relate water-leaving radiance (L_w) to cloud and glint-foam free L_u (Gordon et al., 1983):

$$L_u(\lambda) = L_r(\lambda) + L_a + t(\lambda)L_w(\lambda) + L_{\text{glint}} \quad (2)$$

where $t(\lambda)$ is the diffuse transmittance of the atmosphere below the aircraft, and L_r , L_a and L_{glint} are the radiance contributions due to Rayleigh/Fresnel, aerosol, and glint, respectively. L_r is derived from radiance phase functions for water molecules that depend on incident solar angles (zenith and azimuth), and Fresnel reflectance estimates (Montes-Hugo et al., 2005). L_a was calculated over clearwater pixels where a minimum water-leaving radiance at 665 nm is expected:

$$L_a = W(\lambda_i, \lambda_o)(L_u(665) - L_r(665)) \quad (3)$$

$$W(\lambda_i, \lambda_o) = \varepsilon(\lambda)F_o(\lambda) / F_o(665) \quad (4)$$

$\lambda_o = 665 \text{ nm}$ and $\lambda_i = 412, 443, 491, 509$, and 553 nm . Assuming a maritime atmosphere, ε is 1 (Gordon et al., 1983). $F_o(\lambda)$ is the instantaneous extraterrestrial solar irradiance (ozone optical thickness = 0) (Neckel & Labs, 1984).

Glint contribution to L_u after Hydrolight-based pre-screening of L_u measurements was quantified with a first-order adjustment by subtracting $L_u(780)$ from L_u (Lee et al., 2001). Skylight path radiance contribution was not accurately quantified due to the lack of sky-looking radiance sensor but it was assumed small due to the relatively thin atmospheric layer between the airplane and the sea surface. In this study, ignoring atmospheric contributions to L_u may result in L_w overestimation of up to 70% in shorter wavelengths (e.g., $\lambda = 443 \text{ nm}$) due mainly to molecular backscattering, and 48% at longer wavelengths (e.g., $\lambda = 553 \text{ nm}$) because of the larger influence of aerosols.

Assuming a negligible attenuation of E_d due to the atmospheric path below the airplane, $R_{rs}(\lambda, 0_+)$ was derived as $L_w(\lambda)$ divided by $E_d(\lambda)^{\text{airplane}}$ (cosine of zenith angle = 1) (Montes-Hugo et al., 2005). In case 1 waters, $R_{rs}(\lambda, 0_+)$ can be approximately related (~20% bias) to inherent optical properties of the water body with the following expression (Gordon et al., 1988):

$$R_{rs}(\lambda, 0_+) \approx 0.54 R / Q \quad (5)$$

$$R / Q = 0.095 \{b_b(\lambda) / (b_b(\lambda) + a(\lambda))\} \quad (6)$$

where b_b includes light backscattering contributions due to seawater and particulates, a includes light absorption contributions due to seawater, colored dissolved organic matter and particulates, and R/Q is a shape distribution factor that is influenced by the light field geometry.

2.6. Comparisons of optical parameters derived from passive and active airborne sensors

One important goal of this study was to understand how information provided by passive and active optical sensors was related despite the differences in spatial (i.e., vertically integrated from MicroSAS versus vertically-resolved from FLOE) and spectral (e.g., multi-wavelength MicroSAS versus single-wavelength FLOE) resolution.

Remote sensing reflectance is an apparent optical property (AOP) that is affected by light field angular characteristics such as solar zenith angle. Therefore, a more direct way to evaluate the effects of water characteristics on MicroSAS-derived R_{rs} and FLOE-derived S measurements independently from illumination effects is to use R_{rs} spectral bands and curvature ratios (Montes-Hugo et al., 2005). A preliminary sensitivity analysis suggested two main MicroSAS-derived variables: $R_{rs}(443, 0_+)/R_{rs}(490, 0_+)$ (hereafter R_1) and $R_{rs}(508, 0_+)/R_{rs}(553, 0_+)$ (hereafter R_2). Interestingly, R_1 is inversely related to the average size of particulates of a specific water parcel (Gordon & Morel, 1983) while R_2 is inversely related to the concentration of pigmented particulates containing chlorophyll a (Montes-Hugo et al., 2005).

The comparisons between passive and active optical measurements were organized according to three main questions: How do the

magnitude of MicroSAS and FLOE optical parameters vary? (I), How does α relate to MicroSAS-derived IOPs? (II), What is the depth of the lidar scattering layer having the largest influence on the magnitude and spatial variability of MicroSAS-derived IOPs and R_{rs} ratios? (III).

Regarding (I), we calculated the moments around the mean (arithmetic average, standard deviation, skewness and kurtosis) of the R_{rs} ratios and S . Skewness (ψ) and kurtosis (η) represent the third and fourth standardized moments (m), respectively:

$$\psi = \mu_3 / \sigma^3 \quad (7)$$

$$\eta = \mu_4 / \sigma^4 \quad (8)$$

$$\mu_m = \int_{-\infty}^{\infty} (x-\mu)^m f(x) dx \quad (9)$$

where μ is the arithmetic average, σ is the standard deviation, x is the random variable, and $f(x)$ is the continuous univariate probability density function. Large ψ relative to a Gaussian curve ($\psi=0$) corresponds with an 'excess' of signal that may be related to a greater concentration or composition of optical components (e.g., fish species and abundance in lidar waveforms). Likewise, high η with respect to a Gaussian function ($\eta=3$) means that a greater proportion of the variance is concentrated around the mean, and implies a more 'homogeneous' origin of the optical signal.

For each lidar profile, α was derived from the regression slope of neperian log-transformed S as function of depth after automatic and manual deletion of those 1-m vertically integrated lidar returns where S increases with depth. In case where S increased with depth α was not calculated. Automatic pre-screening and QC of S waveforms was made by setting flags every 1-m depth and detecting positive differences of S with depth as the lidar signal propagates deeper in the water column.

The horizontal patchiness of S (hereafter κ) was derived from the slope of the log-transform power spectrum of vertically averaged S (from 2 to 20 m depth) as a function the log-transformed spatial frequency. The coefficient of variation of S (cv) was computed as the standard deviation of the signal without spatial integration divided by the arithmetic average of S . S parameters (i.e., kurtosis, skewness, α , κ , vertically integrated S , and cv) were computed using the full FLOE vertical resolution (i.e., 179 data points per profile) and between 2 and 20 m depth to minimize surface effects caused by air bubbles and large noise contribution beyond lidar penetration depth (i.e., ~10 standard deviation above the lidar noise).

To examine (II), b_b and α coefficients were calculated from MicroSAS-derived R_{rs} at the lidar wavelength. Only MicroSAS data corresponding to lidar profiles with monotonic decrease of S with depth were selected. An updated version of the quasi-analytical algorithm (QAA_v5) was used to convert R_{rs} into IOPs (Lee et al., 2009). Briefly, QAA_v5 protocol has the following calculation modules: 1) R_{rs} just below the sea surface, 2) spectral shape of b_b and particulate backscattering ($b_{bp}(\lambda)$), 3) spectral shape of $a(\lambda)$, and 4) partition of $a(\lambda)$ in detritus and phytoplankton contributions. Based on the NOMAD validation dataset, QAA_v5 can retrieve a 's in the visible range with a coefficient of determination greater than 0.9 and root-mean square difference (log scale) smaller than 0.2 (Lee et al., 2009). Once b_b (532) and a (532) are derived, K_d (532) can be easily estimated for cloud-free skies (Gordon, 1989).

To answer (III), we performed two different analyses. First, MicroSAS-derived IOPs were related to smoothed S curves using vertically integrated 1-m bins ($\sum S(z_{max}) = \text{sum of the product } S \times dz \text{ from vertical layer } i \text{ to } i + DZ$, where z_{max} , dz and DZ are the upper limit of the integral, the depth differential, and the smoothing interval = 1 m, respectively). Lastly, the influence of different vertical shapes of $S(z)$ on MicroSAS-derived R_{rs} was examined based on the

following contrasting cases: 1) 'exponential' versus 'non-exponential' decrease of $\sum S(z_{max})$ with depth, 2) 'deep' (i.e., ≥ 11 m) versus 'shallow' $\sum S(z_{max})$ maximum, 3) 'thick' (i.e., ≥ 5 m) versus 'thin' $\sum S(z_{max})$ maximum, and 4) 'strong' (i.e., $\geq 7 \cdot 10^{-4} \text{ m sr}^{-1}$) versus 'weak' $\sum S(z_{max})$ maximum. These binary categories are defined with respect to the median of the sample and considering profiles with only one $\sum S(z_{max})$ maximum peak between 3 and 20 m in depth. The magnitude of each $\sum S(z_{max})$ maximum (i.e., largest peak height) is relative and defined with respect to a baseline delineated by the exponential decay of the background signal. The width of each $\sum S(z_{max})$ maximum is estimated at the base of the Gaussian-type peak and corresponds to the distance between two intersecting points made by the peak tails and the background signal. Notice that the final number of lidar profiles with different types of $\sum S(z_{max})$ maximum was relatively small due to the reduced number of coincident FLOE–MicroSAS measurements without atmospheric interference (~10% of original dataset). Although FLOE waveforms with a dominant negative exponential term were observed in numerous occasions (e.g., >500 bins), it was decided to use a number of observations comparable to those obtained in the 'non-exponential' $\sum S(z_{max})$ case study to achieve an even weighting during statistical comparisons. Post-comparisons of moments (low and high) around the mean between these lidar profile types and using all 'exponential' samples did not change observed differences between exponential and non-exponential lidar waveforms.

2.7. Statistical analysis

Passive and active airborne spectral optical products were aggregated into 250-m horizontal bins (i.e., 125 FLOE profiles, 22 MicroSAS measurements) before performing spatial correlations and variance decomposition. The choice of 250-m bins was made for several reasons: 1) It is the best resolution of satellite ocean color sensors with relatively short (1 to several days) revisiting time (e.g., MODIS), 2) The sample size per bin is relatively large (FLOE: $N=125 \times 200$, MicroSAS: $N=360$) for histograms and statistical tests, and 3) Smaller bin sizes would be more influenced by small-scale surface effects (e.g., glint, bubbles due to wave breaking), producing more noise/signal since these surface contributions cannot be completely corrected. The sensitivity of the along-track variability of IOPs to horizontal changes of vertically integrated S (i.e., $\sum S(z_{max})$) was quantified using principal component analysis (PCA) (Pearson, 1901). The contribution of each variable to the first 3 orthogonal axes (i.e., those who explain >80% of total variance) was interpreted based on the loading of each variable to each eigenvector (i.e., principal component or PC). Fraction of total variability explained by principal components decreases from PC1 to PC3. For each eigenvector, the sign of the loading of each optical parameter was used to establish the sign of the correlation (i.e., direct or inverse) between MicroSAS and FLOE variables. The intensity of the relationships between MicroSAS and FLOE optical variables were measured using Spearman Rank non-parametric correlation coefficients (ρ_s) (Spearman, 1904). Comparisons were only performed using a spatial lag equal to zero due to lidar data gaps (e.g., FLOE profiles between 21:20 and 22:33 GMT) along the flight track. Correlations were also examined between different characteristics (amplitude, g_1 , depth, g_2 , and width, g_3) of S waveforms having a single sub-surface peak. Assuming a Gaussian model (G), the relationship between g_1 , g_2 and g_3 is:

$$G(z) = g_1 e^{-0.5((z-g_2)/g_3)^2} \quad (10)$$

The amplitude coefficient is sometimes expressed as $h/(2\pi g_3)$, where h is the total vertically integrated value of the property above a baseline (Millán-Núñez et al., 1997).

The significance of change in the averaged spectral ratios and lidar-derived parameters with different vertical S distributions (see Section 2.6) was evaluated at a confidence interval of probability of 95% and 99% and based on t-Student comparisons with 1-tail. The null hypothesis was $\mu_{\text{group 1}} = \mu_{\text{group 2}}$, with group 1,2...n equal to different subsets of optical data corresponding to pre-defined $S(z)$ clusters. Change of skewness and kurtosis in each dataset was measured with respect to a Gaussian distribution. ψ or η were significant with a 5% error (Type I) when their absolute magnitude was greater than two standard errors of ψ ($\text{ses} = \sqrt{6/N}$, where N =number of observations) and η ($\text{sek} = \sqrt{24/N}$), respectively (Tabachnick & Fidell, 1996). Differences in the coefficient of variation of S per bin between two case studies with N observations (i.e., N_1 and N_2) were examined by comparing a pair of proportions (i.e., p_1 and p_2) with a one-side t-test ($|t| = \sqrt{N_1 N_2 / (N_1 + N_2)} |p_1 - p_2| / \sqrt{pq}$), $p = (p_1 N_1 + p_2 N_2) / (N_1 + N_2)$, $q = 1 - p$, degrees of freedom = $N_1 + N_2 - 2$ (STATISTICA software).

3. Results

3.1. Correspondence between magnitude and spatial variability of spectral reflectance ratios and lidar backscattering signal

Based on spectral ratios of remote sensing reflectance, the color of the ocean was correlated with the magnitude of lidar signal extinction and degree of S patchiness along the horizontal component (Table 1). A typical example showing the coupling between passive and active optical information at different horizontal spatial scales (16 to 250 m) is illustrated in Fig. 2. The airborne measurements were obtained nearby Whale Island (58.00° N, –152.74° W, Fig. 1) at 22:36 h GMT and over relatively deep waters (bottom depth = 120 m). In general, R_1 had a closer association with fine structure changes on 2-D distributions of S (i.e., lidargrams) than did R_2 (Fig. 2a). Likewise, the highest R_1 values commonly coincided with lidar shots characterized by drastic attenuation with depth and where surface (0–5 m depth)

scattering layers were discontinuous (e.g., lidar returns at 1.23 and 3.1 km with respect to the starting distance of the lidargram) (Fig. 2a, d). Conversely, lower R_1 values consistently followed deepening of a mid-water (5 to 15 m depth) scattering layer with an S magnitude comparable to surface values (i.e., $> 1 \cdot 10^{-5} \text{ m}^{-1} \text{ sr}^{-1}$). At a coarser horizontal spatial resolution (i.e., 250 m), the median and standard deviation of R_1 still evidenced the presence of this submerged scattering feature (Fig. 2b). This high reflective 'thin' layer (thickness ~1.5 m) became shallower at the end of the lidar sampling segment (i.e., 3.7 to 4.1 km) and caused a drastic increase of R_1 sd (up to 33-fold) and cv (up to 24-fold). In contrast, minimum R_1 sd ($< 5 \cdot 10^{-3}$) and cv ($< 0.5\%$) were associated with lidar profiles having a monotonic decrease of S with depth (0 to 0.5 km) or relatively weak ($\sim 1.5 \cdot 10^{-7} \text{ m}^{-1} \text{ sr}^{-1}$) and deep (14–16 m depth) scattering layers (e.g., 2 to 2.5 km). Interestingly, maximum values of higher moments around R_1 mean evidenced a horizontal shift of 250

Table 1

Correlation (ρ_s) between airborne passive and active optical parameters. Definitions of I, II and III comparisons are defined in Section 2.6 of Methods. ρ_s significant at 95% ($P < 0.05$) and 99% ($P < 0.01$) confidence level.

Comparison	MicroSAS variables	MicroSAS histogram metrics	FLOE variables	FLOE histogram metrics	ρ_s	P
I	R_1	\bar{x}	$\sum S(20)$		–0.06	0.48
	R_1	\bar{x}	α	\bar{x}	0.38	<0.001
	R_1	\bar{x}	κ	\bar{x}	–0.31	<0.001
	R_2	\bar{x}	$\sum S(20)$		0.15	0.08
	R_2	\bar{x}	α	\bar{x}	–0.07	0.42
	R_2	\bar{x}	κ	\bar{x}	0.18	0.06
	R_1	sd	$\sum S(20)$		0.36	<0.001
	R_1	sd	α	\bar{x}	0.32	<0.001
	R_1	sd	κ	\bar{x}	0.10	0.28
	R_2	sd	$\sum S(20)$		0.20	0.04
	R_2	sd	α	\bar{x}	0.37	<0.001
	R_2	sd	κ	\bar{x}	–0.06	0.54
II	$b_b(532)$	\bar{x}	α	\bar{x}	0.15	0.10
	$a(532)$	\bar{x}	α	\bar{x}	0.11	0.23
	$K_d(532)$	\bar{x}	α	\bar{x}	0.09	0.32
	$b_b(532)$	\bar{x}	$\sum S(3)$		–0.09	0.32
III		\bar{x}	$\sum S(5)$		–0.11	0.23
		\bar{x}	$\sum S(10)$		–0.07	0.41
		\bar{x}	$\sum S(15)$		–0.15	0.10
		\bar{x}	$\sum S(20)$		–0.41	<0.001
	$a(532)$	\bar{x}	$\sum S(3)$		–0.05	0.56
		\bar{x}	$\sum S(5)$		–0.08	0.37
		\bar{x}	$\sum S(10)$		–0.02	0.81
		\bar{x}	$\sum S(15)$		–0.09	0.29
		\bar{x}	$\sum S(20)$		–0.43	<0.001

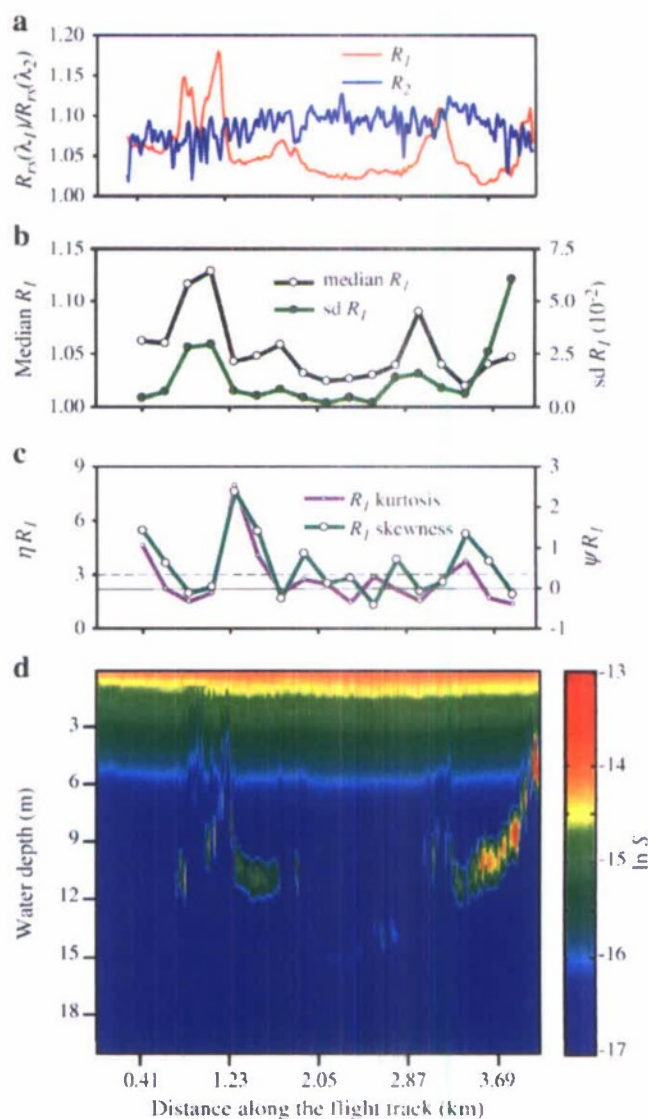


Fig. 2. Spatial relationship between airborne remote sensing reflectance ratios (R_1 and R_2) and vertical distribution of lidar backscattering along the flight track. a) R_{rs} ratios calculated every 16 m, b) \bar{x} and sd of R_{rs} ratios calculated every 250 m, c) same as b) but for kurtosis and skewness, Gaussian kurtosis (dotted line) and skewness (solid line), d) lidar-derived S profiles, S in neperian log scale, distance between profiles is 2 m.

Table 2

Principal component analysis between passive and active optical measurements. In bold are indicated those variables with the largest contribution to each eigenvector (i.e., $\geq |0.3|$).

Sensor	Variables	Histogram metrics	PC1	PC2	PC3
MicroSAS	b_b (532)	\bar{x}	0.16	0.39	-0.55
	a (532)	\bar{x}	0.11	0.41	-0.55
FLOE	$\sum S$ (3)		0.26	-0.53	-0.26
	$\sum S$ (5)		0.20	-0.55	-0.37
	$\sum S$ (10)		-0.46	-0.08	-0.30
	$\sum S$ (15)		-0.44	-0.16	-0.28
	$\sum S$ (20)		-0.38	-0.21	-0.14

to 500 m with respect to R_1 median and sd (Fig. 2c). Roughly, the largest kurtosis and skewness of R_1 tended to lead peaks on R_1 median and sd but this was not always the case (e.g., $\eta = 4.6$, $\psi = 1.42$, median $R_1 = 1.06$, std $R_1 = 4 \cdot 10^{-3}$, first bin centered at 0.41 km).

R_1 - α relationships suggested a strong association between waters dominated by small-sized particulates and greater vertical attenuation of the lidar signal ($\rho_s = 0.38$). As inferred from κ , greater horizontal patchiness of lidar backscattering was associated with water containing larger particles (ρ_s for $R_1 - \kappa = -0.31$). The total strength of the lidar signal integrated from 2.1 to 20 m was not significantly correlated with any spectral R_{rs} ratio. However, the magnitude of $\sum S$ appeared to be related to the horizontal homogeneity of R_1 and R_2 within each bin (Spearman rank correlations between standard deviation of R_{rs} ratios and $\sum S$ up to 0.36). No spatial coherence was detected between magnitude of MicroSAS-derived IOPs and lidar attenuation coefficient values ($P > 0.05$, Table 1). Neither were magnitudes of R_{rs} -based IOPs explained by the magnitude of differences on S at depths above 20 m. Inverse relationships between MicroSAS and FLOE optical signatures were clearly manifested at 20 m depth where correlations between b_b (532), a (532) and S were negative (comparison III in Table 1).

In this study we applied PCA to identify major sources of spatial variability affecting concurrent FLOE and MicroSAS measurements (Table 2). The first Principal component (i.e., PC1) was mainly affected by variability of the 'deep' (10–20 m depth) lidar backscattering. Unlike PC1, PC2 and PC3 were mainly affected by variations on radiometer-derived IOPs and vertically integrated lidar volume backscattering near the surface (3 to 5 m). In PC2, an inverse relationship between passive (b_b (532), a (532)) and active ($\sum S$ at 3 and 5 m depth) parameters suggests that horizontal changes of IOPs were not associated with inter-bin changes of lidar attenuation (i.e., α). PC3 revealed the linkage between of MicroSAS-derived IOPs and lidar volume backscattering at intermediate depths (≥ 3 and ≤ 10 m).

Interestingly, b_b (532) and a (532) had comparable contributions to PC3, which indicates a modulation of lidar signal variability due to spatial fluctuations of both backscattering and absorption coefficients.

3.2. Changes on ocean color statistical moments due to different 'shapes' on lidar waveforms

Spatial patterns of R_{rs} ratios measured in this study differ depending on the number of lidar derived backscattering layers with depth. One single layer with a homogeneous composition of optical constituents (i.e., S only dominated by one exponential decay term) extending from the sea surface down to 20 m typically corresponded to averaged higher R_1 ($t = -5.95$, $P < 0.01$), and higher kurtosis and skewness of R_1 ($\eta = 3.20$, $\psi = 0.19$) than a vertical multi-layered system of S where the amplitude of lidar signal varied with depth (Table 3, Fig. 2c–d). Waters without sub-surface S 'bumps' also had on average 2-fold lower integrated S over the lidar penetration range ($t = 5.3$, $P < 0.01$). In general, lidar profiles with more complex vertical structure produced S with larger coefficient of variability (cv) ($t = 8.95$, $P < 0.01$) and higher κ values ($t = 10.46$, $P < 0.01$) (Table 3).

In general, locations with deeper S peaks (smoothed to 1-m vertical \times 250 m horizontal resolution) had lower horizontal dispersion (i.e., cv) ($t = 3.16$, $P < 0.01$) of targets contributing to S (Table 4). These S distributions tended to be more leptokurtic and symmetric, and commonly associated with larger R_1 kurtosis and negative R_1 skewness. The group of lidar profiles classified by 'weak' sub-surface maxima shared various characteristics of the 'deep' cluster. Within the 'weak' lidar peak category, R_1 histograms had lower skewness ($t = -2.58$, $P = 0.02$), the total integrated S between 2.1 and 3 m was 62% smaller ($t = -3.0$, $P < 0.01$), and the S distribution was less patchy ($t = -1.85$, $P = 0.04$) and more homogenous (i.e., lower cv) horizontally ($t = -4.90$, $P = 0.03$) than the 'strong' cluster. For those lidar profiles with a sub-surface S peak relatively narrow ('thin' scenario), R_1 was higher ($t = 2.0$, $P = 0.03$), R_2 was lower ($t = 1.8$, $P = 0.045$), S vertically integrated per bin tended to be lower ($\sim 30\%$), S skewness was close to zero, and horizontal distribution of S was less patchy than the 'thick' type lidar peak cluster. Overall, depth and magnitude of S sub-surface peaks were inversely correlated ($\rho_s = -0.48$, $t(N-2) = -2.52$, $P = 0.02$) (Appendix A, Table A1).

4. Discussion

Finding relationships between optical properties derived from R_{rs} (λ , 0+) and lidar profiles is an important step forward to elucidate 1) the effects of vertical structure on ocean color imagery and satellite-derived products, and 2) the composition of the lidar signal. The main results of this contribution were organized in two sections: A) How

Table 3

Airborne reflectance derived parameters over waters with A_{01} relatively constant (HS) or varying with depth (IS); min and max are minimum and maximum values, respectively. R_1 , R_2 , κ , and cv (dimensionless), b_b (532), a (532) and K_d (532) (m^{-1}), $\sum S$ ($m sr^{-1}$) 10^{-3} , α (m^{-1}).

		R_1	R_2	b_b (532)	a (532)	K_d (532)	$\sum S$	α	κ	cv
HS	min	1.01	0.68	0.003	0.06	0.09	3.52	0.13	0.03	0.03
	max	1.39	2.33	0.011	0.60	0.87	7.08	0.23	1.37	0.18
	n			41	41	41	41	41	41	41
	\bar{x}	1.18	1.16	0.006	0.16	0.24	5.08	0.18	0.56	0.07
	η	3.20 ± 1.87	2.76 ± 1.46				7.74 ± 4.51			
	ψ	0.19 ± 0.96	0.10 ± 1.27				0.23 ± 0.59			
IS	min	0.96	1.07				4.16		0.62	0.05
	max	1.14	1.33				24.17		2.21	1.62
	n	23	23	23	23	23	23		23	23
	\bar{x}	1.04	1.22				10.11		1.51	0.58
	η	0.27 ± 0.68	2.43 ± 0.83				6.59 ± 6.48			
	ψ	-0.21 ± 1.21	-0.02 ± 0.45				0.64 ± 0.96			

Table 4

Airborne reflectance derived parameters over waters with typical 'shallow', 'deep', 'weak', 'strong', 'thin' and 'thick' lidar profile categories (Section 2.6). Between parentheses is the number of bins used in each lidar profile category.

Category	Histogram metrics	MicroSAS variables	Histogram metrics	FLOE variables		
'Shallow' (11)	$\bar{x} \pm sd$	R_1	1.05 ± 0.06	$\bar{x} \pm sd$	$\sum S$	10.8 ± 6.4
	$\eta \pm sd$	R_1	0.15 ± 0.81	$\eta \pm sd$	S	3.03 ± 4.11
	$\psi \pm sd$	R_1	0.31 ± 0.88	$\psi \pm sd$	S	0.82 ± 1.15
	$\bar{x} \pm sd$	R_2	1.20 ± 0.05	$\bar{x} \pm sd$	κ	7.05 ± 11.00
	$\eta \pm sd$	R_2	2.38 ± 0.62	$\bar{x} \pm sd$	cv	0.99 ± 0.33
	$\psi \pm sd$	R_2	-0.07 ± 0.43			
'Deep' (12)	$\bar{x} \pm sd$	R_1	1.04 ± 0.05	$\bar{x} \pm sd$	$\sum S$	9.5 ± 1.8
	$\eta \pm sd$	R_1	0.37 ± 0.55	$\eta \pm sd$	S	9.87 ± 6.65
	$\psi \pm sd$	R_1	-0.69 ± 1.31	$\psi \pm sd$	S	0.48 ± 0.78
	$\bar{x} \pm sd$	R_2	1.23 ± 0.07	$\bar{x} \pm sd$	κ	1.50 ± 0.44
	$\eta \pm sd$	R_2	2.48 ± 1.00	$\bar{x} \pm sd$	cv	0.37 ± 0.22
	$\psi \pm sd$	R_2	0.03 ± 0.49			
'Weak' (10)	$\bar{x} \pm sd$	R_1	1.05 ± 0.06	$\bar{x} \pm sd$	$\sum S$	7.5 ± 1.7
	$\eta \pm sd$	R_1	0.28 ± 0.64	$\eta \pm sd$	S	8.69 ± 7.33
	$\psi \pm sd$	R_1	-0.87 ± 1.17	$\psi \pm sd$	S	0.20 ± 0.81
	$\bar{x} \pm sd$	R_2	1.21 ± 0.08	$\bar{x} \pm sd$	κ	1.50 ± 0.49
	$\eta \pm sd$	R_2	2.36 ± 1.11	$\bar{x} \pm sd$	cv	0.39 ± 0.26
	$\psi \pm sd$	R_2	-0.05 ± 0.44	$\bar{x} \pm sd$		
'Strong' (13)	$\bar{x} \pm sd$	R_1	1.04 ± 0.05	$\bar{x} \pm sd$	$\sum S$	12.1 ± 5.1
	$\eta \pm sd$	R_1	0.26 ± 0.73	$\eta \pm sd$	S	4.98 ± 5.50
	$\psi \pm sd$	R_1	0.30 ± 1.00	$\psi \pm sd$	S	0.99 ± 0.96
	$\bar{x} \pm sd$	R_2	1.22 ± 0.05	$\bar{x} \pm sd$	κ	4.98 ± 5.50
	$\eta \pm sd$	R_2	2.49 ± 0.56	$\bar{x} \pm sd$	cv	0.81 ± 0.41
	$\psi \pm sd$	R_2	0.01 ± 0.49	$\bar{x} \pm sd$		
'Thin' (9)	$\bar{x} \pm sd$	R_1	1.08 ± 0.06	$\bar{x} \pm sd$	$\sum S$	6.8 ± 4.6
	$\eta \pm sd$	R_1	0.01 ± 0.71	$\eta \pm sd$	S	5.03 ± 5.04
	$\psi \pm sd$	R_1	-0.49 ± 1.57	$\psi \pm sd$	S	0.10 ± 1.09
	$\bar{x} \pm sd$	R_2	1.18 ± 0.06	$\bar{x} \pm sd$	κ	1.56 ± 6.49
	$\eta \pm sd$	R_2	2.34 ± 0.64	$\bar{x} \pm sd$	cv	0.70 ± 0.54
	$\psi \pm sd$	R_2	-0.07 ± 0.36	$\bar{x} \pm sd$		
'Thick' (14)	$\bar{x} \pm sd$	R_1	1.03 ± 0.04	$\bar{x} \pm sd$	$\sum S$	11.1 ± 4.5
	$\eta \pm sd$	R_1	0.44 ± 0.63	$\eta \pm sd$	S	8.29 ± 5.25
	$\psi \pm sd$	R_1	-0.17 ± 1.02	$\psi \pm sd$	S	0.71 ± 0.94
	$\bar{x} \pm sd$	R_2	1.23 ± 0.06	$\bar{x} \pm sd$	κ	4.41 ± 9.31
	$\eta \pm sd$	R_2	2.53 ± 0.96	$\bar{x} \pm sd$	cv	0.50 ± 0.28
	$\psi \pm sd$	R_2	0.01 ± 0.52			

strong is the relationship between total lidar volume backscattering (magnitude and spatial variability) and IOPs (e.g., b_b and a coefficients) as estimated by passive optical systems?, and B) Can we obtain information about vertical shape of profiles based on higher statistical moments of airborne-derived R_{rs} (λ , 0+) (e.g., skewness, kurtosis)?

4.1. Spatial changes on IOPs and vertical attenuation of lidar backscattering

The two-way propagation of lidar signal through a finite aqueous optical path involves attenuation of photons due to particulate and dissolved components (see exponential term in Eq. (1)). Our results suggested that MicroSAS-derived IOPs (a (532) and b_b (532) coefficients, and K_d (532)) were weakly correlated (ρ_s up to +0.15, $P=0.10$) with lidar attenuation coefficient. Based on the FLOE field of view, α can be approximated by K_d (532) (Churnside et al., 1998), thus α is expected to be primarily influenced by absorption of the lidar signal with depth due to background optical constituents (e.g., phytoplankton). That was not the case as R_2 , an index of phytoplankton pigment concentration, was uncorrelated with α (Table 2). Therefore, a greater phytoplankton absorption of green light (i.e., wavelength = 532 nm) did not appear to be a major factor influencing the lidar signal extinction. However, based on principal component analysis (PC3, Table 2), it can be said that spatial variability of α , b_b , and K_d derived at a single wavelength covaried with each other but there were other factors affecting these relationships in the first two orthogonal PCA axis. These additional factors may include differences in polarization between sensors (e.g., cross polarized in FLOE, and

unpolarized in MicroSAS) and phase function variations caused by different illumination geometries (e.g., lidar beam normal to the sea surface versus zenith angle of sunlight rays). Also, some assumptions like vertical homogeneity of IOP distributions and a constant A_{β} (z) may not be valid in some cases, and may introduce bias on K_d and α estimates due to different vertical structure of optical properties. More research will clarify based on our optical system whether the observed poor K_d - α dependency is related to the presence of IOPs inhomogeneities and A_{β} changes along the vertical component and/or to variations inherent to each optical sensor.

Despite the relatively weak connection between magnitude of R_{rs} -derived IOPs and integrated lidar backscattering, higher α or $\sum S$ values were associated with a large variability of R_1 and R_2 within a bin (Table 1). In NGOA waters and during the same period of the year, Brown et al. (2002) concluded that spatial variability of lidar signal appeared to increase with zooplankton density due to a higher degree of spatial patchiness and variation in zooplankton density within patches. Greater spatial variability on zooplankton distributions has been reported in regions characterized by patchy distribution of food (e.g., phytoplankton) (Folt & Burns, 1999). Therefore, a larger spatial heterogeneity of phytoplankton and other particulates affecting R_{rs} ratios can be expected in those waters characterized by more heterogeneous spatial distribution patterns of zooplankton. The impact of zooplankton (i.e., an important optical component affecting S) on phytoplankton (i.e., an important optical component affecting R_{rs} ratios) was presumably evidenced by principal component analysis. The inverse relationship between IOPs and $\sum S$ eigenvector's loadings in PC2 was probably indicative of phytoplankton depletion and consequently a reduction due to zooplankton

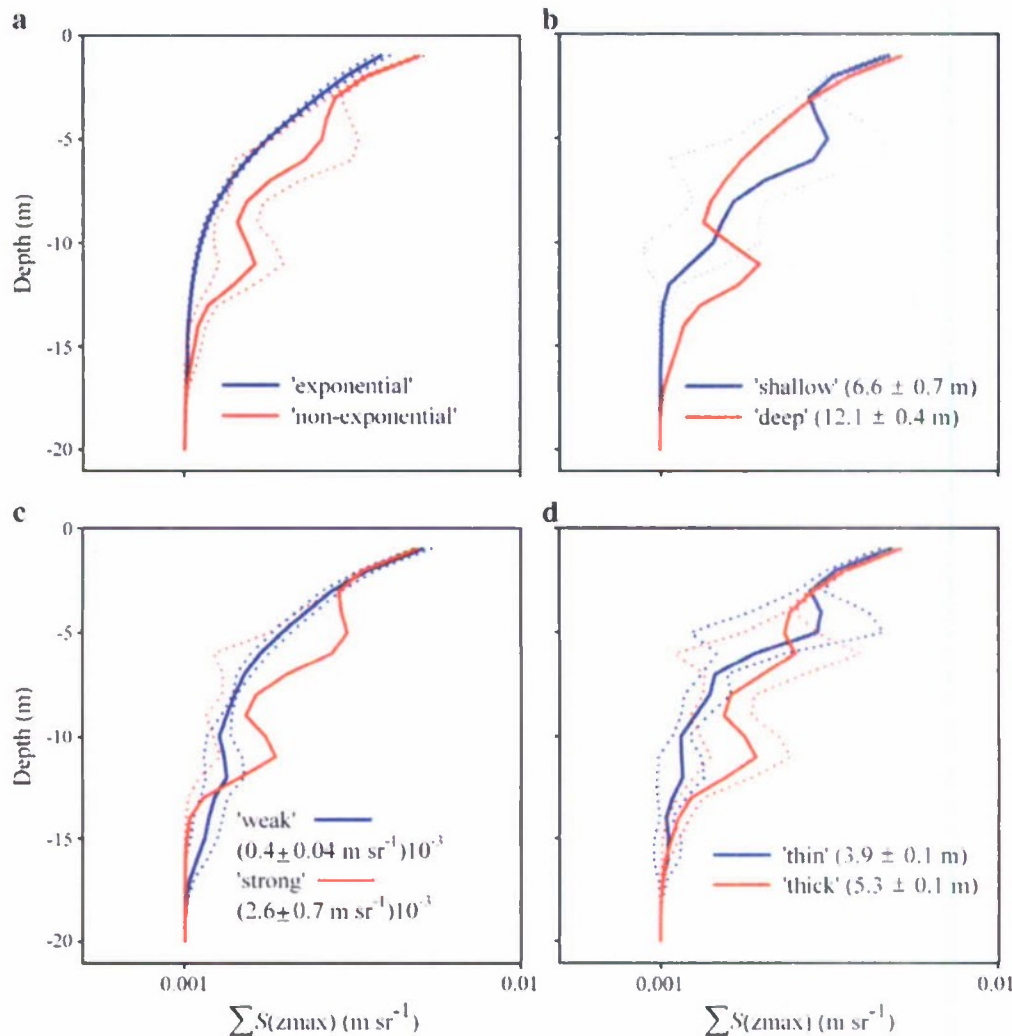


Fig. 3. Classification of lidar waveforms with a single sub-surface S peak. a) 'Exponential' versus 'non-exponential' decrease of S with depth, b) 'shallow' versus 'deep', c) 'weak' versus 'strong', and d) 'thin' versus 'thick'. \bar{x} (solid line) and ± 2 standard errors (se) (dotted line) of each S profile smoothed every 1 m. Between parentheses is $\bar{x} \pm \text{se}$ of each peak. The x-axis is in log scale with base 10 and $\Sigma S(z_{\text{max}})$ values were offset in $+0.001$ to plot $\bar{x} - 2 \text{ se} < 0$.

grazing. ΣS calculated at 3 and 5 m depths suggested that this effect was in part propelled by feeding activity of surface zooplankton layer between dawn and dusk. However during the day, vertical migrating zooplankton (e.g., copepods) like those inhibiting NGOA are preferentially situated in deeper waters (negative loadings of ΣS to PC1 between 10 and 20 m in depth). Thus, a major factor defining IOPs decrease due to ΣS increase was likely the feeding activity of zooplankton during the previous night when a larger volume of grazers was closer to the ocean surface. Spatial variations of the production of pigmented particulates and dissolved colored compounds affecting a and b_b coefficients did not appear to be a major mechanisms explaining magnitude of α or ΣS values since direct relationships between these parameters were secondary as evidenced in PC3.

4.2. Response of spectra reflectance ratios to variation on vertical 'shape' of lidar waveforms

Spatial patterns of ocean color in our study area changed if sub-surface exponential decline of S as a function of depth was interrupted by high scattering layers. This phenomenon was particularly intriguing when analyzing the horizontal shift between maximum of low

(median and sd) and high (η and ψ) moments of R_1 (Fig. 2c–d). It is suggested that spatial lagging of maximum η and ψ was indicative of horizontal 'transitions' of the scattering layer leading to changes on depth, amplitude and thickness of sub-surface S layers. Based on numerical experiments, Carpenter et al. (2009) proposed that drastic temporal variations of skewness and kurtosis can reflect dominance transitions in phytoplankton communities.

Detailed analysis of lidar profile 'shape' parameters derived from sub-surface S peaks and R_{rs} -ratio statistics showed that R_1 skewness was sensitive to deepening of sub-surface S maximum. In general, lidar profiles characterized by a single S sill above the water baseline had more left-skewed R_1 distributions (i.e., more negative ψ) when this shape feature was located far from the sea surface. Based on light propagation models, Kerfoot et al. (2005) calculated a higher R_1 when *Karenia brevis*, a phototactic dinoflagellate, was concentrated near the ocean surface (0–2 m depth). This R_1 increase was likely reflecting a vertically integrated ocean color signal dominated by particles smaller than *K. brevis*. As large cells ($>20 \mu\text{m}$) of *K. brevis* migrate down during morning (5 to 12 am) and late evening (7 pm to 5 am), R_1 decreases reflecting a re-distribution of the surface layer composed by 'large' dinoflagellate-derived particles throughout the water column.

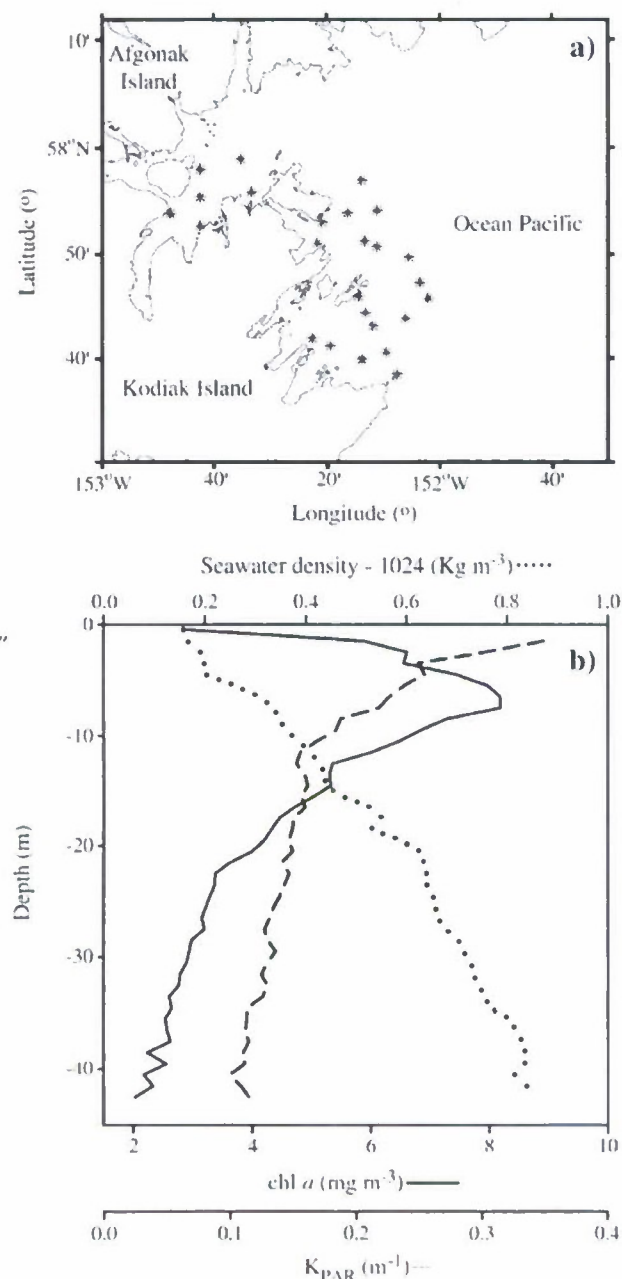


Fig. A1. Vertical structure of density and optical properties during August 2002. a) Geographic location of ship-based sampling stations (asterisks), b) chl *a*, K_{PAR} , and seawater density.

In NGOA waters during summer of 2002, ocean color statistics based on R_{rs} ratios were not better predictors of g_2 than g_1 and g_3 (see Eq. (10), Table 4). This limitation was somehow evidenced by those studies modeling deep chlorophyll *a* maximum (DCM) based on satellite-derived chlorophyll *a* concentration (Millán-Núñez et al., 1997; Sathyendranath et al., 1995).

As expected, parallel changes on higher statistical modes of R_{rs} ratios and $\sum S$ between lidar profiles with contrasting vertical shapes were also accompanied by modifications on lidar κ and cv . In average, lidar waveforms with sub-surface Gaussian peaks had circa of one order of magnitude higher power spectrum slope of S (arithmetic average of $\kappa = 4.15 \pm 7.9$, (1 standard deviation)) and coefficient of variation per bin (250 m horizontal \times 18 m vertical) with respect to those lidar profiles with monotonic decrease of S with depth (Fig. 3).

Table A1
Correlation (ρ_s) between 'shape' parameters describing lidar waveforms with a single sub-surface backscattering maximum.

Comparison	ρ_s	n^a	$t(n-2)$	P
g_2 versus g_1	-0.48	23	-2.52	0.02
g_2 versus g_3	0.28	23	1.35	0.19
g_1 versus g_3	0.35	23	1.72	0.10

^a n is equal to the number of observations, $t(n-2)$ is the Student *t*-test statistics, ρ_s is significant at 95% confidence level when $P < 0.05$.

Considering all lidar profiles obtained during August 17 2002 survey, our arithmetic average κ was 0.61 ± 0.44 (1 standard deviation) and significantly lower with respect to the mean value (1.49 ± 0.03 , near surface returns neglected) reported by Churnside and Wilson (2006) based on FLOE measurements off the coast of Oregon and Washington during July of 2003. As pointed out by Churnside and Wilson (2006) most of our κ values indicate that lidar backscattering patches were smaller with respect to those patches generated by turbulence within the inertial subrange or Brownian motion ($\kappa = 1.67$ to 2.0) but larger with respect to spatial fluctuations equally distributed in terms of amplitude (i.e., $\kappa = 0$ for white noise). Lower S patchiness in this study (i.e., higher κ) with respect to that observed by Churnside and Wilson (2006) can be attributed to a multiplicity of factors including differences of plankton communities, water stratification, primary productivity, and vertical migration patterns between sampling locations.

5. Conclusions

Relationships between vertical structure of optical properties and surface ocean color information were intensively studied during the 1990s using ocean color imagery and ship-based measurements (Millán-Núñez et al., 1997; Sathyendranath et al., 1995). More recently, the optical structure of the ocean interior has been mainly investigated using in-water unmanned sensors (e.g., gliders, Hodges & Frantantoni, 2009; AUVs, Sullivan et al., 2009).

In this work, we propose an alternative approach using high resolution active (lidar) and passive (ocean color radiometer) optical remotely sensed data. Briefly, we propose the use of low and high statistical moments of R_1 to detect S changes along the vertical component. Locations characterized by maximum values of S toward the sea surface were generally associated with R_1 spatial distributions characterized by relatively high arithmetic average, standard deviation, kurtosis and skewness. Conversely, lidar waveforms with additional sub-surface backscattering features tended to have lower arithmetic average, standard deviation, kurtosis and skewness of R_1 . Whether these optical functionalities between active and passive measurements hold in other marine regions or other periods of the year is a matter that deserves more study.

In this study, we demonstrated that passive and active optical measurements can be connected based on a single wavelength (i.e., $\lambda = 532$ nm) even though the apparent lack of correlation between α and MicroSAS-derived optical properties. The observed relationships between R_{rs} ratios and lidar parameters were influenced by additional variables that would require additional experiments involving characterization of optical targets, different lidar polarizations and sunlight geometries, and simultaneous *in situ* measurements of vertical distribution of IOPs.

Observed optical relationships derived from this study represent a preliminary step to better describe thin layers and DCM dynamics, and help improve QC of ocean color products, at least in coastal waters such as those observed in this study, waters characterized by stratified conditions, well defined lidar backscattering layers (i.e., magnitude of S maximum comparable to near surface values), and relatively high vertically integrated chl *a* (>150 mg m^{-2}) within the euphotic zone.

Acknowledgements

This work was supported by the NRL internal project "3D Remote Sensing with a Multiple-Band Active and Passive System: Theoretical Basis", PE0601153N. We thank the captain and crew of the FV Laura of Kodiak, the pilot of the aircraft, and Tim Veenstra at Airborne Technologies Inc. (Wasilla, Alaska).

Appendix A. Ship-based profiles of oceanographic variables

Shipboard profiles of downwelling photosynthetically available radiation (PAR) were conducted aboard FV Laura of Kodiak Island and during August 16–18 of 2002. The summer survey consisted in 26 vertical casts encompassing a depth range between 50 and 198 m (Fig. A1a). Surface ($E_d(\text{PAR}, 0+)$) and underwater ($E_d(\text{PAR}, 0-)$) PAR measurements were collected with a Biospherical Instruments, Inc., PRR 2600 profiling reflectance radiometer system. Raw $E_d(\text{PAR}, 0-)$ profiles were quality checked by removing spikes and values increasing with depth caused by temporal variation of near surface (e.g., wave focusing) and above surface (e.g. cloudiness) environmental factors. *A posteriori*, downcast $E_d(\text{PAR}, 0-)$ profiles were smoothed every meter based on arithmetic averaging, and vertically diffuse attenuation coefficient of PAR (K_{PAR}) was calculated assuming an exponential decrease (neperian base) of PAR with depth (e.g., $K_{\text{PAR}}(z_2) = -\log(E_d(\text{PAR}, 0-)/E_d(\text{PAR}, 0-)) / (z_2 - z_1)$).

Temperature, practical salinity, chlorophyll *a* fluorescence and water depth were recorded with a Sea-Bird Electronics, Inc., model 25–143 CTD. Pre-cruise CTD calibrations were performed at Sea-Bird lab (temperature accuracy $\pm 0.002^\circ\text{C}$, practical salinity accuracy ± 0.005). Magnitude of chl *a* was estimated from fluorescence measurements (Seapoint fluorometer, excitation wavelength = 470 nm, emission = 685 nm, sensitivity = 0.02 mg m^{-3} , and temperature stability of $<0.2\%/^\circ\text{C}$). The Seapoint sensor was calibrated in the lab with a Turner Designs Model 10-AU fluorometer and using the non-acidification method (Welschmeyer, 1994). In general terms, the median of CTD-derived variables in shelf waters of Afognak/Kodiak Islands evidenced stratified conditions characterized by a developed pycnocline in the first 10 m of the water column (i.e., vertical seawater density changes $>0.02 \text{ kg m}^{-3}$) associated with drastic increase ($>100\%$) of K_{PAR} above that depth and larger chl *a* toward a water depth of 7 m (up to 8.2 mg m^{-3}) (Fig. A1b).

References

- Brown, E. D., Churnside, J. H., Collins, R. L., Veenstra, T., Wilson, J. J., & Abnett, K. (2002). Remote sensing of capelin and other biological features in the North Pacific using lidar and video technology. *ICES Journal of Marine Science*, 59, 1120–1130.
- Carpenter, S. R., Brock, W. A., Cole, J. J., & Pace, M. L. (2009). Leading indicators of phytoplankton transitions caused by resource competition. *Theoretical Ecology*, 2, 139–148.
- Churnside, J. H., Tatarskii, V. V., & Wilson, J. J. (1998). Oceanographic lidar attenuation coefficients and signal fluctuations measured from a ship in the Southern California Bight. *Applied Optics*, 37, 3105–3112.
- Churnside, J. H., & Wilson, J. J. (2006). Power spectrum and fractal dimension of laser backscattering from the ocean. *Journal of the Optical Society of America*, 23, 2829–2833.
- Churnside, J. H., & Wilson, J. J. (2008). Ocean color inferred from radiometers on low-flying aircraft. *Sensors*, 8, 860–876.
- Churnside, J. H., Wilson, J. J., & Tatarskii, V. V. (2001). Airborne lidar for fisheries applications. *Optical Engineering*, 40, 406–414.
- Folt, C. L., & Burns, C. W. (1999). Biological drivers of zooplankton patchiness. *Trends in Ecology & Evolution*, 14, 300–305.
- Gordon, H. W. (1982). Interpretation of airborne oceanic lidar: Effects of multiple scattering. *Applied Optics*, 21, 2996–3001.
- Gordon, H. R. (1989). Dependence of diffuse reflectance of natural waters on the sun angle. *Limnology and Oceanography*, 34, 1484–1489.
- Gordon, H. R., & Brown, O. B. (1975). Diffuse reflectance of the ocean: Some effects of vertical structure. *Applied Optics*, 14, 2892–2895.
- Gordon, H. R., Brown, O. B., Evans, R. E., Brown, J. W., Smith, R. C., Baker, K. S., et al. (1988). A semi-analytic model of ocean color. *Journal of Geophysical Research*, 93, 10909.
- Gordon, H. R., Clark, D. K., Brown, J. W., Brown, O. B., Evans, R. H., & Broenkow, W. W. (1983). Phytoplankton pigment concentrations in the middle Atlantic bight: Comparisons between ship determinations and coastal zone color scanner estimates. *Applied Optics*, 22, 20–36.
- Gordon, H. R., & Morel, A. (1983). *Remote assessment of ocean color for interpretation of satellite visible imagery: A review*. New York: Springer-Verlag 1983.
- Hodges, B. A., & Frantantoni, D. M. (2009). A thin layer of phytoplankton observed in the Philippine Sea with a synthetic moored array of autonomous gliders. *Journal of Geophysical Research*, 114. doi:10.1029/2009JC005317
- Kerfoot, J., Kirkpatrick, G., Lohrenz, S., Mahoney, K., & Schofield, O. (2005). Vertical migration of a *Korenia brevis* bloom: Implications for remote sensing of harmful algal blooms. In K. A. Steidinger, J. H. Landserber, C. R. Tomas, & G. A. Vargo (Eds.), *Harmful Algae 2002: Proceedings of the 10th International Conference of Harmful Algae* (pp. 279–283). St. Petersburg, Florida, USA: Florida Fish and Wildlife Commission, Florida Institute of Oceanography and Intergovernmental Oceanographic Commission of UNESCO 2004.
- Lee, Z., Carder, K. L., Chen, R. F., & Peacock, T. G. (2001). Properties of the water column and bottom derived from Airborne Visible Infrared Imaging Spectrometer (AVIRIS) data. *Journal of Geophysical Research*, 106, 11639–11651.
- Lee, Z., Lubac, B., Werdell, J., & Arnone, R. (2009). An update of the quasi-analytical algorithm (QAA_v5) International Ocean Color Group software report. www.ioccg.org/groups/Software/OCA.
- Millán-Núñez, R., Alvarez-Borrego, S., & Trees, C. C. (1997). Modeling the vertical distribution of chlorophyll in the California Current System. *Journal of Geophysical Research*, 102, 8587–8595.
- Mitchell, J. G., Yamazaki, H., Seuront, L., Wolk, F., & Li, H. (2008). Phytoplankton patch patterns: Seascape anatomy in a turbulent ocean. *Journal of Marine Systems*, 69, 247–253.
- Montes-Hugo, M., Carder, K., Foy, R., Cannizzaro, J., Brown, E., & Pegau, S. (2005). Estimating phytoplankton biomass in coastal waters of Alaska using airborne remote sensing. *Remote Sensing of Environment*, 98, 481–493.
- Morel, A. (1991). Light and marine photosynthesis: A spectral model with geochemical and climatological implications. *Progress in Oceanography*, 26, 263–306.
- Neckel, H., & Labs, D. (1984). The solar radiation between 3300 and 12500 Å. *Solar Physics*, 90, 205–258.
- Pearson, K. (1901). On lines and planes of closest fit to systems of points in space. *Philosophical Magazine*, 2, 559–572.
- Piskozub, J., Neumann, T., & Woźniak, L. (2008). Ocean color remote sensing: Choosing the correct depth weighting function. *Optics Express*, 16, 14683–14688.
- Platt, T., Sathyendranath, S., Caverhill, C. M., & Lewis, M. R. (1988). Ocean primary production and available light: Further algorithms for remote sensing. *Deep-Sea Research*, 35, 855–879.
- Prieur, L., & Sathyendranath, S. (1981). An optical classification of coastal and oceanic waters based on the specific spectral absorption curves of phytoplankton pigments, dissolved organic matter, and other particulate materials. *Limnology and Oceanography*, 26, 671–689.
- Sathyendranath, S., Longhurst, A., Caverhill, C. M., & Platt, T. (1995). Regionally and seasonally differentiated primary production in the North Atlantic. *Deep-Sea*, 42, 1773–1802.
- Smith, R. C., & Baker, K. S. (1981). Optical properties of the clearest natural waters (200–800 nm). *Applied Optics*, 20, 177–184.
- Spearman, C. (1904). The proof and measurement of association between two things. *American Journal of Psychology*, 15, 72–101.
- Sullivan, J. M., Donaghay, P. L., & Rines, J. E. B. (2009). Coastal thin layers dynamics: Consequences to biology and optics. *Continental Shelf Research*, 30, 50–65.
- Tabachnick, B. G., & Fidell, L. S. (1996). *Using multivariate statistics* (3rd ed.). New York, Harper Collins (eds).
- Welschmeyer, N. A. (1994). Fluorometric analysis of chlorophyll *a* in the presence of chlorophyll *b* and phaeopigments. *Limnology and Oceanography*, 39, 1985–1992.
- Westberry, T. K., & Siegel, D. A. (2006). Spatial and temporal distribution of *Trichodesmium* blooms in the world's oceans. *Global Biogeochemical Cycles*, 20, gb4016. doi:10.1029/2005GB002673
- Zanaveld, R. (1982). Remotely sensed reflectance and its dependence on vertical structure: A theoretical derivation. *Applied Optics*, 21, 4146–4150.